Color correction of texture images for true photorealistic visualization

Yonghak Song, Jie Shan *

Geomatics Engineering, School of Civil Engineering, Purdue University, 550 Stadium Mall Drive, West Lafayette, IN 47907, USA

ARTICLE INFO

ABSTRACT

Photorealistic visualization combines 3-D geometric models with their texture images to render the virtual world. This paper points out that the texture images should be radiometrically corrected to achieve a true realistic appearance. Such a correction should include not only the color adjustment among images of the same object, but also the shade variation caused by the illumination change. The objective of this study is to correct the input texture images such that their shade varies when being rendered under different illumination directions. To achieve this goal we first apply the specular-to-diffuse mechanism based on the dichromatic reflection model to remove the specular component from the texture image. The resultant diffusion-only image then undergoes a shade correction to produce a normalized shade-free texture image. In the final step, shades under any illumination are produced to achieve a true photorealistic effect. Presented in the paper are the principles and methods for such corrections, along with a performance evaluation based on the graphic and numerical results for roof texture images.

1. Introduction

Photorealistic visualization combines 3-D geometric models with their texture images to render the virtual world. This process provides a realistic perception and is becoming a popular functionality for geospatial exploration (Döllner et al., 2006). Recently, a photorealistic visualization over urban areas is of particular interest and challenge due to the complexity and variety of urban features (Varshosaz, 2003). This is more obvious for large scale visualization, where man-made features need to be presented in great detail at a high resolution. The state-of-the-art of the technologies makes it possible to map building roof and façade texture images onto the geometric models in an automated or semi-automated manner. However, at least two problems have not been sufficiently addressed so that a perfect photorealistic visualization can be achieved. First, the images used for texture mapping may likely be collected at different locations and angles and even with different sensors. Objects made of the same materials usually do not have exactly the same appearance or color due to a number of reasons such as illumination direction, camera pointing, specular reflection, sensor noise, and environmental noise. Such "*internal differences*" can even be observed among the different primitives of an object in a single image. These internal differences among images are often corrected during the production of the image mosaics by adjusting their colors using various radiometric correction methods such as

multi-resolution spline convolution (Burt and Adelson, 1983), histogram matching (Du et al., 2001; Zheng et al., 2006), weighted-blending (Nicholas, 2001), and polygon based blending (Tsai et al., 2005). The other problem is related to rendering. When a photorealistic model is rendered under an illumination direction other than the one from which the texture images were taken, the view should appear different from the original texture images, i.e., a new shade effect will occur. This phenomenon is primarily caused by the difference between the real illumination direction and the rendering illumination direction, and thus is named as "*external difference*" here for briefness. An ideal photorealistic view should not only perform a color adjustment between images, but also change the color of the texture images according to the rendering illumination direction.

The above two problems are generally referred to as color correction in this paper and should be resolved to achieve a high fidelity true photorealistic visualization. It should be pointed out that this concept is an extension to the classical geometric correction that only changes the geometry of the image in the process of rectification or rendering. It is also a conceptual generalization from the ordinary color adjustment where color differences among the images of the same scenes are minimized. The color correction in this paper will change the radiometry or color of the texture images such that they are mutually consistent and also vary with the change of the illumination directions. Such combined geometric and radiometric corrections form a comprehensive concept for a true photorealistic visualization.

This study addresses two issues in the color correction: specular removal and shade correction. The texture image records the electromagnetic energy reflected from the object. It consists of two

* Corresponding author.
E-mail address: jshan@ecn.purdue.edu (J. Shan).

components: specular reflection and diffusion reflection. Specular reflection is a surface phenomenon. Even for significantly rough surfaces, specular reflection is observed at the specular direction and may cause an erroneous result in image segmentation and shading analysis. Hence, the specular reflection is undesirable and needs to be removed (Nayer et al., 1993). This is a classical topic in computer graphics (Shafer, 1985) and many efforts exist to remove the confounding effect of the illumination sources so that the corrected texture image contains only the color of the object. In addition, to carry out the shade's correction, the specular effect should be first removed from the texture image, which therefore becomes the first task in this study.

The other component, diffuse reflection, results from the light rays penetrating the object surface, undergoing multiple reflections, and re-emerging at the object's surface. It varies slowly and is treated as independent from the viewing direction in some simplified reflection models such as the Lambertian model (Wolff, 1996). The effect of diffuse reflection is the gradual change of intensities over the texture image. Such an effect is also called the shade, which is the change of intensity due to the spatial variation of the object's surface (Finlayson and Schaefer, 2001). Three potential problems for true photorealistic visualization can arise due to the shade. First, it causes objects composed of the same material with an identical color to appear differently in the texture image. The second problem is related to the performance of rendering. Efficient texture mapping should be able to balance between the rendering speed and the rendering details, and not all details are needed for rendering (Heckbert, 1986). Hence, the shade in the texture images of the same material should be generated to form one "normalized" texture image that can be used for multiple roofs made of the same material. The third problem is that the shade needs to be changed when the model is rendered from an illumination direction different than the one in which the texture images were taken. Our second task is therefore to correct the shades of the same material to a normalized shade and change (transform) it according to the illumination direction when being rendered.

The remainder of the paper first discusses the principles of specular removal and the shade's correction. Relevant studies in computer graphics and remote sensing are reviewed for each topic. The study then uses color images of building roofs to demonstrate the presented principles and methodology. Both the graphic and numerical results are presented to evaluate the performance of this study.

2. Specular reflection removal

As was addressed earlier, the intensity of a texture image has two components: specular reflection and diffuse reflection. Separating the specular component from the texture image is necessary for photorealistic visualization and is also a prerequisite for the shade's correction. This is a topic that has been extensively studied in computer graphics with most of the effort based on the dichromatic reflectance model (Shafer, 1985). Utilizing this model, Klinker et al. (1988) observed that the color histogram of an object with a uniform diffuse color presents a T-shape with two limbs, respectively corresponding to the diffuse component and the specular component. However, this T-shape is rarely separable for most real images due to the existence of noise (Klinker et al., 1988). Bajcsy et al. (1990) showed additional limbs produced by interreflections between objects. They suggested that the separation should be performed in the space of brightness, saturation and hue. Although it was more accurate, it needed the correct specular-diffuse pixel segmentation. Lee (1992) used a "moving sensor" method and applied spectral differencing to the color histograms of the consecutive images for the specular component extraction. More recently, Tan et al. (2004) proposed a separation method

based on the distribution of specular and diffuse points or pixels in a two-dimensional maximum chromaticity-intensity space. Our study in this paper adopts and applies this method. However, for a consistency of discussion and the convenience of readers, it will be presented below along with derivations and an example of the implementation. For the complete original work, see Tan et al. (2004).

The dichromatic reflection model (Shafer, 1985) is composed of two additive components, diffuse reflection and specular reflection

$$\mathbf{I}(\mathbf{x}) = w_d(\mathbf{x})\mathbf{D}(\mathbf{x}) + w_s(\mathbf{x})\mathbf{S}(\mathbf{x}) \tag{1}$$

where

$\mathbf{I} = \{I_r, I_g, I_b\}^T$: the color vector of the image's intensity, where the subscripts r, g, b respectively stand for the red, green and blue components.

$\mathbf{x} = \{x, y\}$: the image's coordinates.

$\mathbf{D}(\mathbf{x}), \mathbf{S}(\mathbf{x})$: the diffuse reflection vector and the specular reflection vector.

$w_d(\mathbf{x}), w_s(\mathbf{x})$: weighting factors for the diffuse and specular components.

According to Tan and Ikeuchi (2005), the diffuse reflection is due to the varying refractive indices in the object's surfaces, while the specular reflection is mainly due to the refractive index difference between the object surface and the air. The values of the weighting factors depend on the geometric structure of the object at the location $\mathbf{x}$.

Next, the concept of chromaticity is introduced, which in general is defined as a normalized vector (Tan et al., 2004).

$$\begin{aligned}
\boldsymbol{\sigma}(\mathbf{x}) &= \frac{\mathbf{I}(\mathbf{x})}{I_r(\mathbf{x}) + I_g(\mathbf{x}) + I_b(\mathbf{x})} \\
\boldsymbol{\lambda}(\mathbf{x}) &= \frac{\mathbf{D}(\mathbf{x})}{D_r(\mathbf{x}) + D_g(\mathbf{x}) + D_b(\mathbf{x})} \\
\boldsymbol{\gamma}(\mathbf{x}) &= \frac{\mathbf{S}(\mathbf{x})}{S_r(\mathbf{x}) + S_g(\mathbf{x}) + S_b(\mathbf{x})}
\end{aligned} \tag{2}$$

$\boldsymbol{\sigma}$ is the chromaticity corresponding to the image's intensity. By inserting the diffuse chromaticity ($\boldsymbol{\lambda}$) and the specular chromaticity ($\boldsymbol{\gamma}$) into Eq. (1), the image's intensity can be expressed as a combination of the diffuse chromaticity and the specular chromaticity

$$\mathbf{I}(\mathbf{x}) = m_d(\mathbf{x})\boldsymbol{\lambda}(\mathbf{x}) + m_s(\mathbf{x})\boldsymbol{\gamma}(\mathbf{x}) \tag{3}$$

where $m_d(\mathbf{x})$ and $m_s(\mathbf{x})$ are the normalized weight factors

$$\begin{aligned}
m_d(\mathbf{x}) &= w_d(\mathbf{x})(D_r(\mathbf{x}) + D_g(\mathbf{x}) + D_b(\mathbf{x})) \\
m_s(\mathbf{x}) &= w_s(\mathbf{x})(S_r(\mathbf{x}) + S_g(\mathbf{x}) + S_b(\mathbf{x})).
\end{aligned} \tag{4}$$

Before the full mathematic development for the specular component removal is presented, its task can be conceptually introduced below. A pixel in an image may belong to one of two types: a diffuse pixel or a specular pixel. A diffuse pixel has no specular component, i.e., $m_s = 0$, which means that its intensity comes entirely from the diffuse reflections of the objects. On the other hand, a specular pixel has both a diffuse component and a specular component, i.e., $m_d > 0$ and $m_s > 0$, which implies that its intensity comes from both a single mirror reflection and multiple diffusion reflections at the object's surface due to its roughness. The task of removing the specular component is to determine the specular contribution, $m_s(\mathbf{x})\boldsymbol{\gamma}(\mathbf{x})$, in Eq. (3) such that it can be subtracted from the image color vector $\mathbf{I}(\mathbf{x})$. The resultant diffuse contribution, $m_d(\mathbf{x})\boldsymbol{\lambda}(\mathbf{x})$, will be the final color vector in the specular-free image.

To calculate the specular component, the concept of chromaticity defined in Eq. (2) is utilized. Since $(\gamma_r + \gamma_g + \gamma_b) = (\lambda_r + \lambda_g + \lambda_b) = (\sigma_r + \sigma_g + \sigma_b) = 1$, inserting Eq. (3) into the $\boldsymbol{\sigma}(\mathbf{x})$ expression in Eq. (2) will yield

$$\boldsymbol{\sigma}(\mathbf{x}) = \frac{m_d(\mathbf{x})\boldsymbol{\lambda}(\mathbf{x}) + m_s(\mathbf{x})\boldsymbol{\gamma}(\mathbf{x})}{m_d(\mathbf{x}) + m_s(\mathbf{x})}. \tag{5}$$
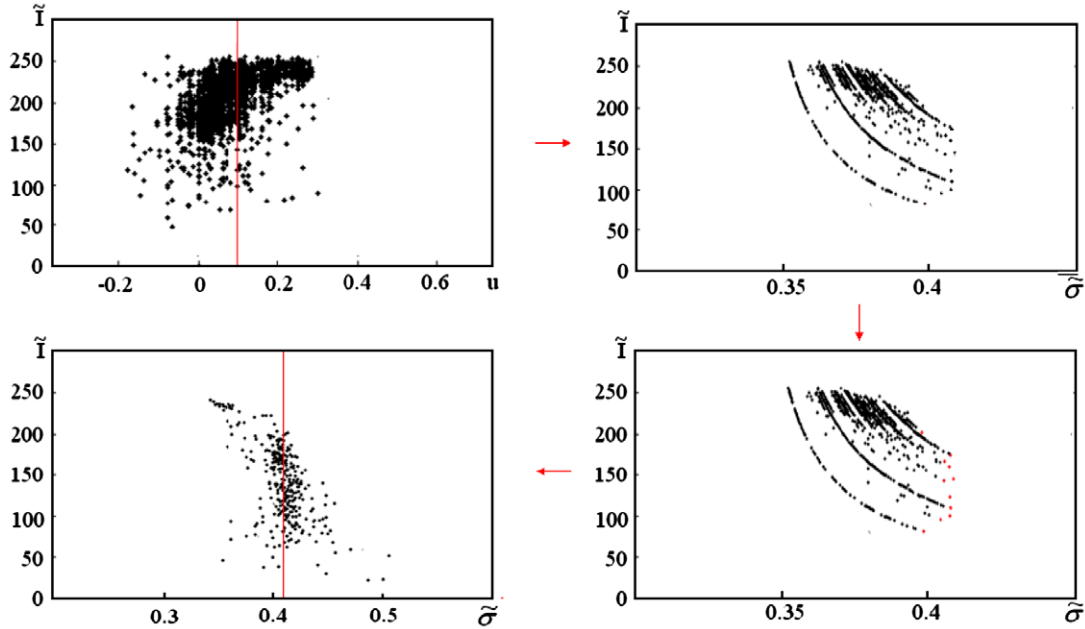
Fig. 1. Steps for determining the maximum chromaticity $\tilde{\sigma}$.

According to Tan et al. (2004), the maximum chromaticity, which essentially identifies the dominant color, is defined as

$$\tilde{\sigma}(\mathbf{x}) = \max\{\sigma_r(\mathbf{x}), \sigma_g(\mathbf{x}), \sigma_b(\mathbf{x})\} = \frac{\tilde{I}(\mathbf{x})}{I_r(\mathbf{x}) + I_g(\mathbf{x}) + I_b(\mathbf{x})} \quad (6)$$

where

$$\tilde{I}(\mathbf{x}) = \max\{I_r(\mathbf{x}), I_g(\mathbf{x}), I_b(\mathbf{x})\}. \quad (7)$$

As $m_d > 0$ and $m_s > 0$, and under the assumption of white illumination, i.e., $\boldsymbol{\gamma}(\mathbf{x}) = (1/3 \quad 1/3 \quad 1/3)^T$, it can be shown that the maximum elements of $\boldsymbol{\sigma}(\mathbf{x})$, $\boldsymbol{\lambda}(\mathbf{x})$, and $\boldsymbol{\gamma}(\mathbf{x})$ occur at the same row or at the same color component (such as red). Let $\tilde{\lambda}(\mathbf{x})$ and $\tilde{\gamma}(\mathbf{x})$, respectively, be the elements in $\boldsymbol{\lambda}(\mathbf{x})$ and $\boldsymbol{\gamma}(\mathbf{x})$ corresponding to $\tilde{\sigma}(\mathbf{x})$ in $\boldsymbol{\sigma}(\mathbf{x})$, then Eq. (5) can be written in the scalar form with the maximum chromaticity $\tilde{\sigma}(\mathbf{x}) = (m_d(\mathbf{x})\tilde{\lambda}(\mathbf{x}) + m_s(\mathbf{x})\tilde{\gamma}(\mathbf{x}))/(m_d(\mathbf{x}) + m_s(\mathbf{x}))$. With rearrangement this will lead to

$$m_s(\mathbf{x}) = m_d(\mathbf{x})\frac{\tilde{\lambda}(\mathbf{x}) - \tilde{\sigma}(\mathbf{x})}{\tilde{\sigma}(\mathbf{x}) - \tilde{\gamma}(\mathbf{x})}. \quad (8)$$

Inserting Eq. (8) into Eq. (3) and considering $\tilde{\gamma}(\mathbf{x}) = 1/3$, we have

$$\tilde{I}(\mathbf{x}) = m_d(\mathbf{x})(3\tilde{\lambda}(\mathbf{x}) - 1)\frac{\tilde{\sigma}(\mathbf{x})}{3\tilde{\sigma}(\mathbf{x}) - 1} \quad (9)$$

or

$$m_d(\mathbf{x}) = \frac{\tilde{I}(\mathbf{x})(3\tilde{\sigma}(\mathbf{x}) - 1)}{\tilde{\sigma}(\mathbf{x})(3\tilde{\lambda}(\mathbf{x}) - 1)}. \quad (10)$$

Once the diffuse weight factor is determined from the last equation, the specular weight factor can be calculated with

$$m_s(\mathbf{x}) = I_r(\mathbf{x}) + I_g(\mathbf{x}) + I_b(\mathbf{x}) - m_d(\mathbf{x}). \quad (11)$$

Finally, the diffuse component, i.e., the specular-free image can be formed by subtracting the specular contribution, $m_s(\mathbf{x})/3$, from the input image $\mathbf{I}(\mathbf{x})$ with the following equation

$$m_d(\mathbf{x})\boldsymbol{\lambda}(\mathbf{x}) = \mathbf{I}(\mathbf{x}) - m_s(\mathbf{x})[1/3 \quad 1/3 \quad 1/3]^T. \quad (12)$$

The above development in Tan et al. (2004) forms the basis of the specular-to-diffuse mechanism for the specular component removal. It is seen that once $\tilde{\sigma}(\mathbf{x})$ and $\tilde{\lambda}(\mathbf{x})$ are determined, Eqs. (10)–(12) can then be used to remove the specular component. Under the assumption that the object's surface in question is made

of the same material and uniform, then both the diffuse and the specular pixels have the same diffuse component,

$$\tilde{\lambda}(\mathbf{x}) = \tilde{\lambda}(\mathbf{x}_d) = \tilde{\sigma}(\mathbf{x}_d) \quad (13)$$

where $\mathbf{x}_d$ stands for the diffuse pixels. Thus, the key in using Eqs. (10)–(12) is to obtain the maximum chromaticity $\tilde{\sigma}$ (omitting the location for simplicity of notations) for the diffuse pixels.

According to Tan et al. (2004), the maximum chromaticity-intensity space $(\tilde{\sigma}, \tilde{I})$ is formed where the horizontal axis represents the maximum chromaticity defined in Eq. (6) and the vertical axis is for the maximum intensity of the color vector defined in Eq. (7). Under the assumption of a uniform surface and a white illumination, the specular pixels should have a larger intensity $(\tilde{I})$ and smaller maximum chromaticity $(\tilde{\sigma})$ than the diffuse pixels due to the maximum operation in the definition of $\tilde{I}$. In addition, the maximum chromaticity $(\tilde{\sigma})$ of the diffuse pixels should be a constant for the uniform object. However, due to the effect of the sensor and the environmental noises, such ideal situation does not occur in real images and one cannot directly separate the two components using the above principle. The suggested procedure by Tan et al. (2004) consists of the following steps. First, we calculate the color index (u).

$$u = \frac{I_r + I_b - 2I_g}{I_g + I_b - 2I_r} \quad (14)$$

for every pixel of the object. This color index is designed such that the effect of the equal specular components will be canceled in a noise-free image and all the pixels from one uniform object should ideally yield a constant u value. To consider the effect of noise, we divide the range of u, (u_{min}, u_{max}), into a number of bins (50 in this study). As shown in Fig. 1, the pixels corresponding to one bin u_i (upper left) are plotted into the maximum chromaticity-intensity space $(\tilde{\sigma}, \tilde{I})$ (upper right). Such a plot will be approximated by a number of straight lines (100 in this study) as an approximation to Eq. (9). The maximum $\tilde{\sigma}$'s of each of the straight lines will be selected as candidates (lower right), yielding 100 $\tilde{\sigma}$'s corresponding to the 100 straight lines. This procedure is repeated for all 50 bins of u and a total of 5000 candidate $\tilde{\sigma}$'s are selected. The final selection of $\tilde{\sigma}$ for the object is determined by forming the
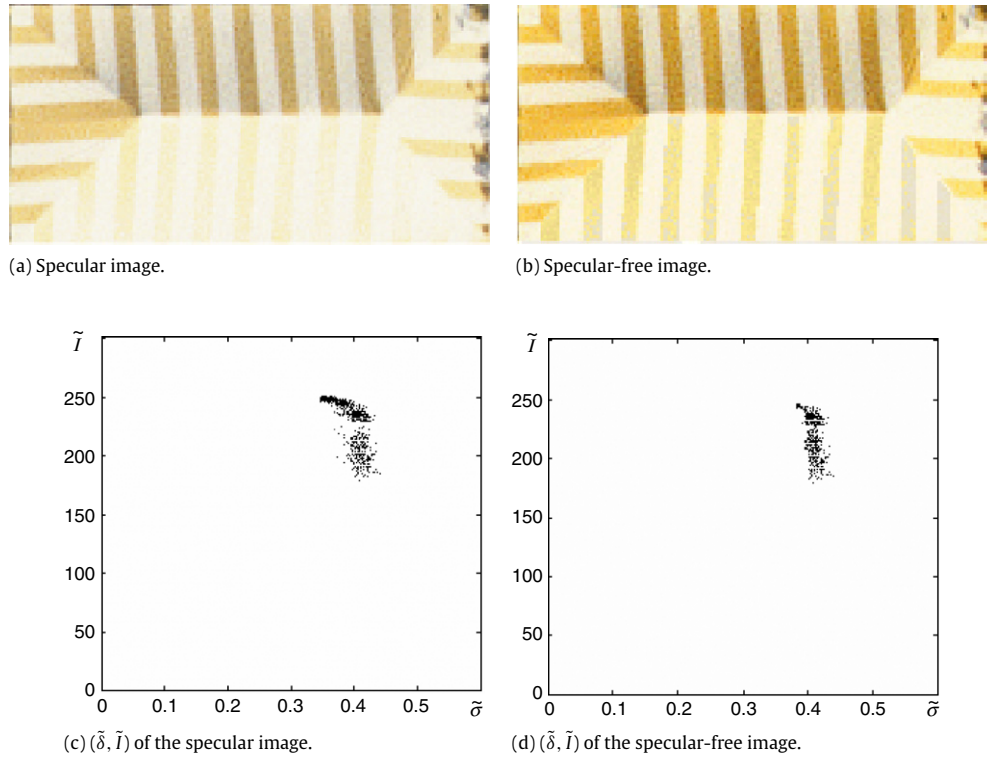
(a) Specular image.

(b) Specular-free image.

(c) $(\tilde{\delta}, \tilde{I})$ of the specular image.

(d) $(\tilde{\delta}, \tilde{I})$ of the specular-free image.

Fig. 2. Specular correction of a tent image.

histogram of $\tilde{\sigma}$'s and selecting the $\tilde{\sigma}$ that has the highest frequency (lower left).

For the purpose of illustration, the above principles and implementation are applied to correct the specular effect on an aerial image of a tent shown in Fig. 2(a). The intermediate steps and results for this correction are depicted in Fig. 1 and the original image and final specular-free image are shown in Fig. 2(a) and (b), respectively. Fig. 2(c) and (d) present the maximum chromaticity-intensity space of the example image before and after the specular correction.

3. Shade correction and transform

Once the specular-free image is obtained, it is ready for a further correction of the shade effect. For this purpose, what is needed is a reflection model that describes the relationship between the shade (image), the object and the incoming light. Remote sensing has used various methods to correct the shade effects caused by the topography. Representative methods include the Lambertian (cosine) correction, the Minnaert correction (Minnaert, 1941; Teillet et al., 1982), and a normalization method (Civco, 1989). Newton et al. (1991) applied a complex and intensive shading model to remove the irradiance variation effects in the Landsat TM imagery using digital elevation models.

This study uses the three popular reflection models: the cosine (Lambertian) model, the Minnaert model, and the Marsik model. All these models need to calculate the incident angle i, i.e., the angle between the illumination normal (O) and the surface normal (S). As shown in Fig. 3, E is the slope inclination, Z is the solar zenith angle, A_o is the solar azimuth, and A_s is the surface aspect of the slope. Under these notations, the unit vector of the solar direction is $[\sin Z \cdot \sin A_o \quad \sin Z \cdot \cos A_o \quad \cos Z]^T$ and the unit vector of the surface normal is $[\sin E \cdot \sin A_s \quad \sin E \cdot \cos A_s \quad \cos E]^T$. The dot product of the two unit vectors leads to the following formula (Holben and Justice, 1980; Smith et al., 1980)

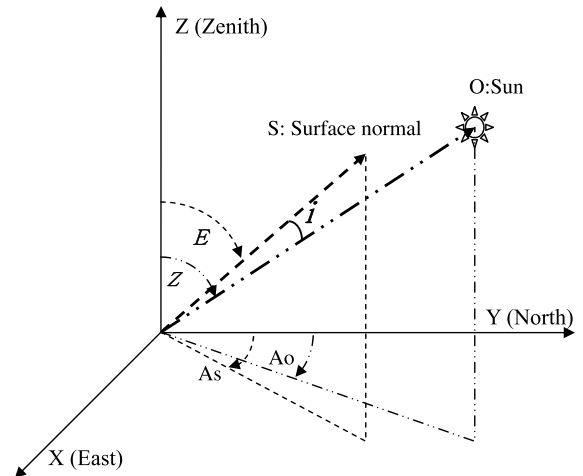$$\cos i = \cos E \cos Z + \sin E \sin Z \cos(A_s - A_o). \tag{15}$$

Fig. 3. Geometry of incident angle calculation.

The Lambertian model assumes that the object's surface is a perfect diffuse reflector, i.e., the same amount of reflectance occurs in all viewing directions. This model can be written as (Teillet et al., 1982; Jones et al., 1988)

$$\mathbf{I}_n = (\mathbf{I}_d - \mathbf{I}_a)/\cos i \tag{16}$$

where $\mathbf{I}_d$ is the color vector of the specular-free or diffuse-only image, $\mathbf{I}_a$ is the constant color vector caused by the ambient light, $\mathbf{I}_n$ is the color vector to be determined for the final shade-free image or a normalized image.

The Minnaert model below was developed for the photometric analysis of the lunar surface in Minnaert (1941)

$$\mathbf{I}_n = \frac{\mathbf{I}_d \cos e}{\cos^k i \cos^k e} \tag{17}$$

where e is the slope angle and k is the Minnaert constant. The model uses the Minnaert constant k to describe the roughness of a

Table 1
Means and color ratios of roofs in one building.

	Roof 1	Roof 2	Roof 3	Roof 4	Roof 5
Mean R	204.3	145.5	192.8	218.3	114.5
Mean G	162.2	104.3	149.1	183.6	113.0
Mean B	138.0	96.4	127.5	160.6	108.5
Color ratio	−0.16	−0.37	−0.20	−0.13	0.41
Incident angle	39.98°	67.75°	56.82°	20.88°	0.23°

surface. For surfaces with a Lambertian behavior, $k = 1$; otherwise, $k < 1$.

The third model is based on the Marsik (1971) method. It takes the form

$$\mathbf{I}_n = \frac{1}{1 + \log(\cos i)}\mathbf{C}_d \otimes \mathbf{I}_d - \frac{1}{1 + \log(\cos i)}\mathbf{C}_a \quad (18)$$

where $-\log(\cos i) = D$ is called the shading density function (Marsik, 1971), $\mathbf{C}_d$ and $\mathbf{C}_a$ are the scale vectors, respectively, for the diffuse light and the ambient light, $\otimes$ stands for the product of the corresponding elements in two vectors.

A shade transform is needed to convert the shade under one illumination direction to the shade under another illumination direction. For this purpose we use the shade-free image of the intermediate step, i.e., the resultant shade-free image created through a shade correction is transformed to form a new shade image. This is the reverse process of the shade correction. The unknown to be determined for shade transform is $\mathbf{I}_d$, while all the other parameters, except the incident angle i, in the above shade models (Eqs. (16)–(18)) are known through the shade correction process.

4. Tests and discussion

This section evaluates the aforementioned principles and methods for the specular removal and the shade correction for generating a true photorealistic effect. The tests are carried out with roof models and roof texture images obtained by aerial photography. The roof images have a pixel size of 30 μm and are obtained by scanning the aerial photographs at a scale of 1:4000. The scanned images have three R, G, B bands with a radiometric scale from 0 to 255 per band. The roof models are digitized roof by roof from a stereo pair. For the simplicity of discussion and to prevent any ambiguity in the context, the term roof here refers to each individual digitized planar face atop a building.

Every individual building is processed with two sequential steps: specular removal and shade correction. After verifying the assumption of white illumination following Tominaga and Wandell (1989), each roof image is separately applied to the specular removal. The pixels of every roof image are treated as one correction unit, for which a maximum chromaticity $\tilde{\sigma}$ is determined. After that, every roof pixel is subject to the specular reflection removal by using Eqs. (10)–(13).

The specular-free images are then used for the shade correction. We first group the roofs of a building according to their color ratios (Eq. (14)) calculated by the mean color components of all pixels in one roof. Roofs with the maximum color ratio difference within ±0.25 (gray value) are regarded as being made of the same material and should have the same reflection properties. As an example, Table 1 lists the mean R, G and B components and the color ratios of the five roofs of a building (Fig. 4). Roofs 1, 2, 3 and 4 are considered to be made of the same material, which is different from the material for roof 5.

The three shading models described in Section 3 are applied to the specular-free images for the shade correction. The solar azimuth and zenith at the time the image was taken are obtained based on the time tag and location of the aerial photograph using the NOAA solar calculator (http://www.srrb.noaa.gov/highlights/sunrise/azel.html). The incident angles are then calculated using

the roof normals with Eq. (15). Every roof within one group will form one set of equations to determine the normalized color $\mathbf{I}_n$ and other parameters $\mathbf{I}_a$ or $\mathbf{C}_a$ and $\mathbf{C}_d$ with a linear regression. The pixel values of the roof images are then adjusted for shade correction by using the resultant model parameters. Fig. 4 shows the shade-corrected roofs with and without specular reflection removal.

For comparison purpose, the shade correction results from both with and without specular reflection removal are presented along with their histograms to show the distribution of the pixel values. The original image and its histogram (C1) in Fig. 4 suggest that the entire building roof has two dominant colors which represent four slant parts (roof 1–4) and one flat part (roof 5). However, the histogram of the original image shows three apparent peaks due to three illuminated slant parts, one shaded slant part and the flat part. A successful specular removal and shade correction should ideally make the two dominant colors more distinct and show only two peaks. The middle (C2) and right columns (C3) show improvement towards this goal. Shade correction increases the separability of the two dominant colors by harmonizing the colors of the roofs made of the same material and thus successfully forming the two more centralized peaks in the histograms. It should be noted, however, that such an improvement is sometimes not apparently visible from the texture images if their specular component is small. Instead, the histograms demonstrate the differences in all three shade correction models.

In order to quantitatively evaluate the performance of the specular and the shade corrections, Table 2 lists the standard deviations of the images for the above four roofs made of the same material. We first calculate the variance of each individual roof (planar face)

$$\sigma_i^2 = \frac{1}{m_i} \sum_{j=1}^{m_i}(g_{ij} - \bar{g}_i)^2 \quad (19)$$

where i and j are the roof and the pixel numbers, respectively; g_{ij} is the pixel value of the j-th pixel of the i-th roof; $\bar{g}_i$ is the mean of the i-th roof; m_i is the number of pixels of the i-th roof. The within-roof variance is the average of the above variances of n individual roofs made of the same material

$$\bar{\sigma}^2 = \frac{1}{n} \sum_{i=1}^{n}\sigma_i^2. \quad (20)$$

On the contrary, the between-roof variance is calculated in a similar way to Eq. (19), however, by taking the mean of the pixels of all the roofs (Eq. (20)). The underlying mechanism for such an evaluation is as follows. Each roof has an intrinsic shade variation due to the material's roughness. This variation is represented by its variance as calculated in Eq. (19). For roofs made of the same material, they should have a similar standard deviation, if the shade and specular effects are corrected. The large variation between the roofs, if any, is caused by the specular reflection and the diffuse reflection. A perfect correction should yield a variance between all roofs made of the same material as close as possible to the variance of each individual roof, i.e., the within-roof variance.

First of all, as depicted in Table 2 (left section), the input images show large between-roof standard deviations, which implies the existence of specular reflection and shade differences among the roofs. Our effort should reduce such between-roof variations, ideally to the within-roof variance, which is intrinsic for the roofs made of the same material. Table 2 (right section) shows the shade correction without the specular correction changes the variation between (as measured by average roof variance) roofs from 38.6 to 10.2 as an average of all three shade correction models. Including the removal of the specular component, though it is small, can further improve the color correction performance from 10.2 to 7.1, which is very close to the average within-roof variation (7.21)
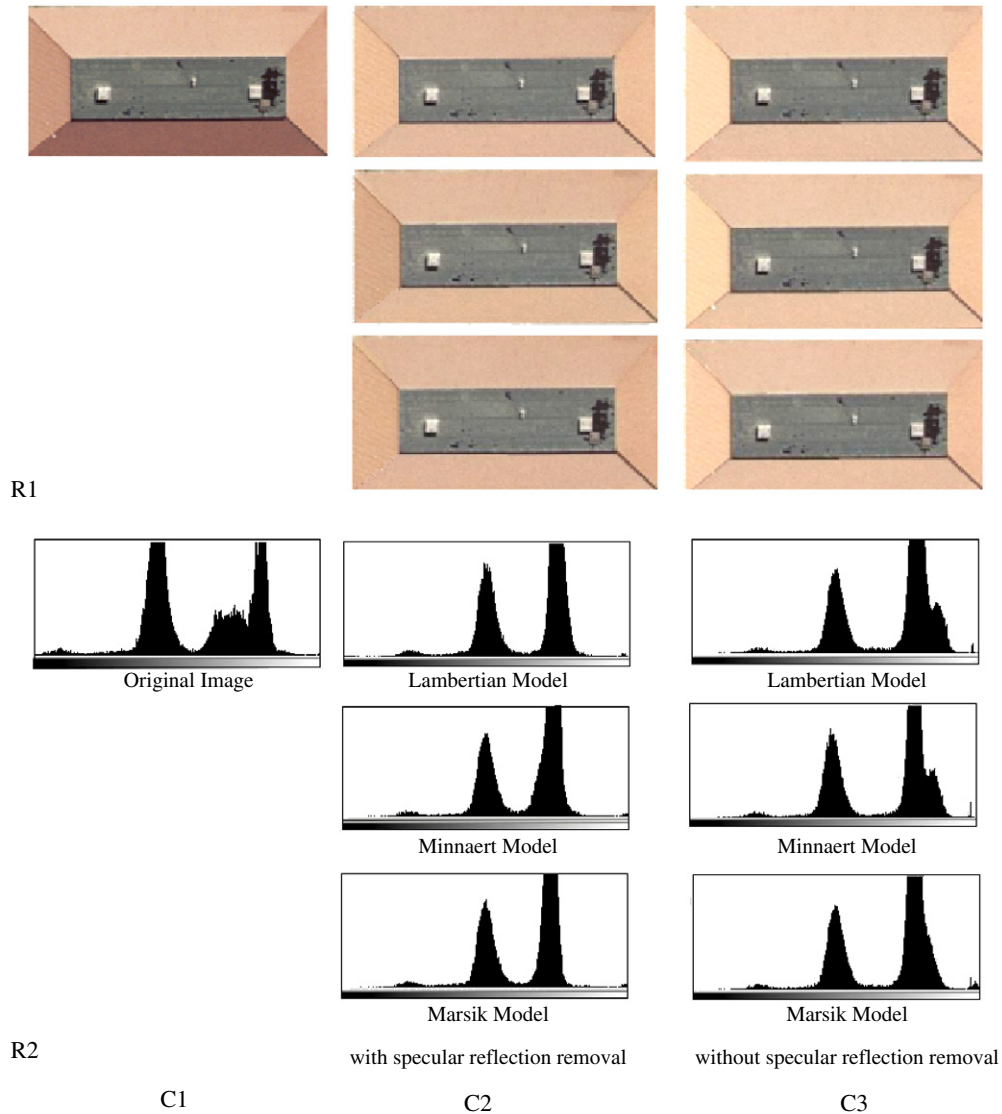
R1

R2

C1   C2   C3

Original Image   Lambertian Model   Lambertian Model

Minnaert Model   Minnaert Model

Marsik Model   Marsik Model

with specular reflection removal   without specular reflection removal

Fig. 4. Shade-corrected images (R1) and intensity histograms (R2) of the red band based on the original image (left column, C1) and different shade correction models for with (middle column, C2) and without (right column, C3) the specular removal.

Table 2
Standard deviations of the input and shade-corrected roof images.

Band	Input image		Shade correction (between roofs)					
	Between roofs	Within roofs	Lambertian		Minnaert		Marsik	
			w/o	w/	w/o	w/	w/o	w/
Red	37.30	6.54	13.37	7.81	10.81	8.29	9.35	6.34
Green	40.52	7.92	11.43	6.84	10.39	8.61	8.29	6.44
Blue	33.48	8.25	9.69	7.09	9.04	8.97	7.99	7.62
Intensity	38.60	7.21	11.59	6.82	10.09	8.27	8.21	6.21

w/o: without specular correction; w/: with specular correction.

in the input images. Such closeness is the optimal performance one can expect in the specular and the diffusion corrections since it harmonizes the roofs made of the same material, while at the same time each individual roof is still perceptible by keeping its intrinsic texture properties embedded in its variance. As for the performance of the individual shade correction model, the Marsik model yields the best results, followed by the Lambertian model and the Minnaert model, although all of them are very similar in this study.

Our final study is about a shade transform, i.e., to generate the texture images under an illumination direction possibly different from the one of the input images. As an evaluation strategy, we first produce the texture images under the illumination direction in which the original images were taken. The reproduced roof images are then compared with the input images, pixel by pixel. Fig. 5 plots the standard deviations of such pixel-by-pixel differences for the three color bands of the four roofs tested above. A perfect shade correction and shade transform process should yield a minimum variation during this forward (correction) and backward (transform) process. According to Fig. 5, the specular correction makes considerable improvement to the straight shade correction, because the specular-free image helps the determination of the parameters in the shade correction models. This further verifies the previous discussion. Finally, it is seen that the differences among
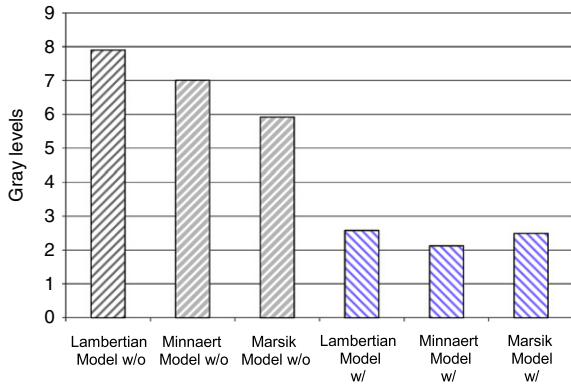
Fig. 5. Standard deviations of the intensity differences between the reproduced roof images and the input roof images, without (left three) and with (right three) specular corrections.

Fig. 6. Shade correction of roof images, 1st column: Original texture image at sun direction (A_s: 161.75°, Z: 46.82°); 2nd column: Shade-free texture image; 3rd column: Texture rendering at sun location (A_s: 341.75°, Z: 46.82°; opposite to the 1st column); 4th column: Texture rendering at the same sun direction as the original image. North is to the right.

the three shade correction methods are as small as only two gray levels.

Figs. 6–8 present the rendered roofs generated by using the Marsik model. In Fig. 6, the original texture images (1st column) are shown beside the corrected shade-free images (2nd column). Through the corrections the input images are normalized to their material color without the specular and the diffuse reflections. The roofs in a building made of the same material have little color variation as is shown in the second column. The third column is the rendering results at the illumination direction opposite to the one of the input image. As is shown, the shade transform thus reverses the brightness of the roofs in the input images. The last column in Fig. 6 is the reproduced input images based on the shade-free images by assuming the illumination direction being the same as the input images. No apparent difference is noticed between the input and its reproduction, illustrating a check on the ability of the shade transform to match the original shade conditions.
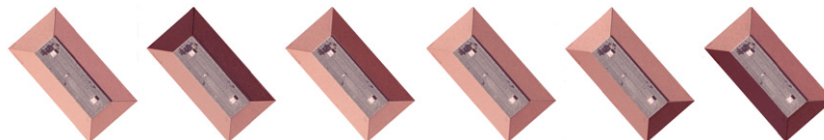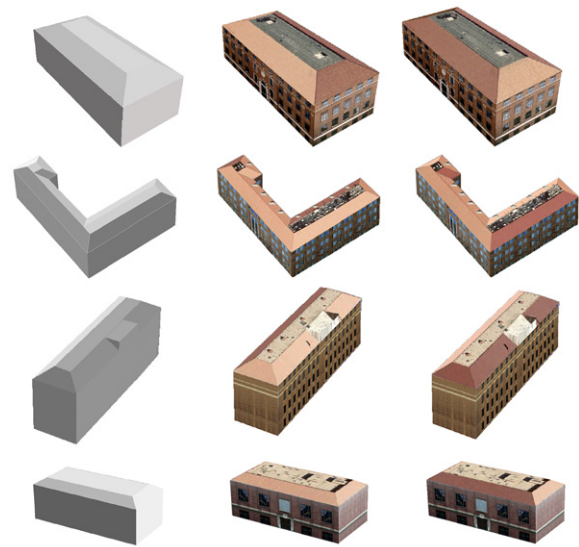

Fig. 8. 3D models and texture mapping: Shaded geometric models (left), roof texture mapping without (middle) and with (right) shade transform.

Fig. 7 simulates the roof shade changing during a day from 7:00 to 15:00 at a two-hour interval. Finally, Fig. 8 presents a number of 3-D building models and their texture rendering results. The first column shows the expected shading effects by using the geometric models under a certain illumination direction. The second column renders the models with textures from the original image without a color correction. It is clear that the input textures do not match the expected shades (first column). The corrected texture images are mapped to the geometric models and their rendering results shown in the third column produce a good match to the desired shade.

5. Conclusion

The concept of photorealistic visualization needs to be extended to include the necessary radiometric corrections to the involved texture images. Such corrections should not only handle the color adjustment among images of the same object, but consider the shade effect caused by variable illumination directions when the model is being rendered. These corrections will lead to the achievement of true photorealistic visualization. This study has addressed the correction of two radiometric effects: the specular reflection and the diffuse reflection. For removal of the specular reflection, the method of Tan et al. (2004) based on the dichromatic reflection model was applied. It was shown that the specular effect was visible either directly in the texture images or indirectly through their histograms. The removal of the specular effect could enhance the contrast of the texture images, and benefit the subsequent shade correction and determination of the shade transform model. In the shade correction and transform steps, the specular-free image was used to create a shade-free or normalized texture image, which is both geometrically and radiometrically corrected. It could then be used to render texture images under any illumination direction different from the one in which the input image was taken. Tests with a number of roof

Fig. 7. Roof rendering at different time of day. The very left is the input image taken at 11:43, October 5, 1999; followed by the rendered images at 7:00, 9:00, 11:00, 13:00 and 15:00. North is to the right.

images demonstrated that both corrections could be implemented effectively without interaction for a given building model. It was shown that although the Marsik model was the best, all of the three tested shade correction models yielded similarly satisfactory rendering results. Finally, the color correction outcome could be quantitatively evaluated by the proposed evaluation metrics based on the between-roof and among-roof variances.

As for future effort, it is necessary to extend our current work on roof images mostly formed of one type of material to more complex objects, such as roofs with different colors and materials. Ground images of building walls and façades shall also be included to further demonstrate the performance and effect of the specular and the shade correction. All this will allow for handling more realistic building images that often consist of more than one material type such as brick, window, door and other decorations. The added realism will essentially demand not only the detailed geometric modeling, but also a comprehensive material modeling of the scene. Finally, the color correction discussed here should be integrated with the visualization tools and the geographic information systems to achieve a true photorealistic effect under flexible illumination directions.

Acknowledgements

References

Bajcsy, R., Lee, S.W., Leonardis, A., 1990. Color image segmentation with detection of highlights and local illumination induced by interreflections. In: Proc. International Conference on Pattern Recognition, vol. 1, Atlantic City, NJ, USA, 16–21 June. pp. 785–790.

Burt, P.J., Adelson, E.H., 1983. A multiresolution spline with application to image mosaics. ACM Transactions on Graphics 2 (4), 217–236.

Civco, D.L., 1989. Topographic normalization of Landsat Thematic Mapper digital imagery. Photogrammetric Engineering & Remote Sensing 55 (9), 1303–1309.

Döllner, J., Kolbe, T.H., Liecke, F., Sgouros, T., Teichmann, K., 2006. The virtual 3D city model of Berlin—Managing, integrating, and communicating complex urban information. In: Proc. 25th Urban Data Management Symposium, Aalborg, Denmark, 15–17 May. pp. 9.73–9.86 (on CD-ROM).

Du, Y., Cihlar, J., Beaubien, J., Latifovic, R., 2001. Radiometric normalization, composition and quality control for satellite high resolution image mosaics over large area. IEEE Transactions on Geoscience and Remote Sensing 39 (3), 623–634.

Finlayson, G., Schaefer, G., 2001. Colour indexing across devices and viewing conditions. In: Proc. 2nd International Workshop on Content Based Multimedia and Indexing, Brescia, Italy, 19–21 September. pp. 215–221.

Heckbert, P.S., 1986. Survey of texture mapping. IEEE Computer Graphics and Applications 6 (11), 56–67.

Holben, B.N., Justice, C.O., 1980. The topographic effects on spectral response from nadir-point sensors. Photogrammetric Engineering & Remote Sensing 46 (9), 1191–1200.

Jones, A.R., Wyatt, B.K., Settle, J.J., 1988. Use of digital terrain data in the interpretation of SPOT-1 HRV multispectral imagery. International Journal of Remote Sensing 9 (4), 669–682.

Klinker, G.J., Shafer, S.A., Kanade, T., 1988. Color image analysis with an intrinsic reflection model. In: Proc. International Conference on Computer Vision, Tampa, FL, USA, 5–8 December. pp. 292–296.

Lee, S.W., 1992. Understanding of surface reflection in computer vision by color and multiple views. Ph.D. Dissertation, University of Pennsylvania, USA.

Marsik, Z., 1971. Automatic relief shading. Photogrammetria 27 (2), 57–70.

Minnaert, M., 1941. The reciprocity principle in lunar photometry. Astrophysical Journal 93, 403–410.

Nayer, S.K., Fang, X., Boult, T., 1993. Removal of specularities using color and polarization. In: Proc. IEEE Computer Vision and Pattern Recognition'93, New York City, USA, 15–17 June. pp. 583–590.

Newton, A., Muller, J.-P., Pearson, J., 1991. SPOT DEM shading for Landsat-TM topographic correction. In: IEEE Geoscience and Remote Sensing Symposium, IGARSS, vol. 2, Espoo, Finland, 3–6 June. pp. 655–659.

Nicholas, H., 2001. New methods for dynamic mosaicking. IEEE Transactions on Image Processing 10 (8), 1239–1251.

Shafer, S.A., 1985. Using color to separate reflection components. Color Research and Applications 10 (4), 210–218.

Smith, J.A., Tzeu, L.L., Ranson, K.J., 1980. The Lambertian assumption and Landsat data. Photogrammetric Engineering & Remote Sensing 46 (9), 1183–1189.

Tan, R.T., Nishino, K., Ikeuchi, K., 2004. Separating reflection components based on chromaticity and noise analysis. IEEE Transactions on Pattern Analysis and Machine Intelligence 26 (10), 1373–1379.

Tan, R.T., Ikeuchi, K., 2005. Separating reflection components of textured surfaces using a single image. IEEE Transactions on Pattern Analysis and Machine Intelligence 27 (2), 178–193.

Teillet, P.M., Guindon, B., Goodenough, D.G., 1982. On the slope-aspect correction of multispectral scanner data. Canadian Journal of Remote Sensing 8 (2), 84–106.

Tominaga, S., Wandell, B.A., 1989. Standard surface reflectance model and illuminant estimation. Journal of the Optical Society of America A 6 (4), 576–584.

Tsai, F., Lou, H., Hsiao, K., 2005. Semiautomatic texture generation and transformation for cyber city building models. In: IEEE Geoscience and Remote Sensing Symposium, IGARSS, vol. 7, Seoul, Korea, 25–29 July. pp. 4980–4983.

Varshosaz, M., 2003. True realistic 3D models of buildings in urban areas. International Archives of Photogrammetry, Remote Sensing and Spatial Information Sciences 34, (Part 5/W10) (on CD-ROM).

Wolff, L.B., 1996. Generalizing Lambert's law for smooth surfaces. In: The Fourth European Conference on Computer Vision, vol. II. European Vision Society, Cambridge, UK, 15–18, April. pp. 40–53.

Zheng, L., Zhang, J., Luo, Y., 2006. Color matching in color remote sensing image. In: First International Multi-Symposiums on Computer and Computational Sciences, IMSCCS'06, vol. 1, Hangzhou, China, 20–24 June. pp. 303–306.